Supplemental Document

optica

Spin-to-orbital angular momentum conversion via light intensity gradient: supplement

SHUANG-YIN HUANG,[1] GUAN-LIN ZHANG,[1] QIANG WANG,[1] MIN WANG,[1] CHENGHOU TU,[1] YONGNAN LI,[1,4] AND HUI-TIAN WANG[2,3,*]

[1] *Key Laboratory of Weak-Light Nonlinear Photonics and School of Physics, Nankai University, Tianjin 300071, China*
[2] *National Laboratory of Solid State Microstructures and School of Physics, Nanjing University, Nanjing 210093, China*
[3] *Collaborative Innovation Center of Advanced Microstructures, Nanjing University, Nanjing 210093, China*
[4] *e-mail: liyongnan@nankai.edu.cn*
[*] *Corresponding author: htwang@nju.edu.cn*

Supplement DOI: https://doi.org/10.6084/m9.figshare.15221787

Parent Article DOI: https://doi.org/10.1364/OPTICA.435475

Spin-to-orbit angular momentum conversion via light intensity gradient

This document provides supplementary information to "Spin-to-orbit angular momentum conversion based on light intensity gradient", giving the details about the theory and the experiment.

1. CALCULATION OF THE OPTICAL ANGULAR MOMENTUM

In the Cartesian coordinate system (x, y), the transverse electric field of optical field with spatial distribution of polarization and phase in free space can be written as

$$\mathbf{E}_{\perp}(x,y) = [E_x(x,y)\hat{\mathbf{e}}_x + E_y(x,y)\hat{\mathbf{e}}_y]\exp(jk_z z - j\omega t). \tag{S1}$$

By $\hat{\mathbf{e}}_x = \cos\varphi\hat{\mathbf{e}}_r - \sin\varphi\hat{\mathbf{e}}_\varphi$ and $\hat{\mathbf{e}}_y = \sin\varphi\hat{\mathbf{e}}_r + \cos\varphi\hat{\mathbf{e}}_\varphi$, in the cylindrical coordinate system (r,φ), Eq. (S1) can be rewritten as

$$\mathbf{E}_{\perp}(r,\varphi) = [(E_x\cos\varphi + E_y\sin\varphi)\hat{\mathbf{e}}_r + (E_y\cos\varphi - E_x\sin\varphi)\hat{\mathbf{e}}_\varphi]\exp(jk_z z - j\omega t). \tag{S2}$$

Here $\hat{\mathbf{e}}_x$ and $\hat{\mathbf{e}}_y$ are the unit vectors in the x and y axes in the Cartesian coordinate system, respectively. $\hat{\mathbf{e}}_r$ and $\hat{\mathbf{e}}_\phi$ are the unit vectors in the radial and azimuthal coordinates in the cylindrical coordinate system, respectively. From the Maxwell's equation $\nabla\cdot\mathbf{E} = 0$ in the dielectric medium, we can give the longitudinal component of electric field as

$$\mathbf{E}_z(r,\varphi) = \frac{j}{k_z}\left[\cos\varphi(\frac{\partial E_x}{\partial r} + \frac{1}{r}\frac{\partial E_y}{\partial\varphi}) + \sin\varphi(\frac{\partial E_y}{\partial r} - \frac{1}{r}\frac{\partial E_x}{\partial\varphi})\right]\exp(jk_z z - j\omega t). \tag{S3}$$

With $\nabla\times\mathbf{E} = -\mu_0\partial\mathbf{H}/\partial t$, the magnetic field $\mathbf{H}$ can be calculated by the electric field $\mathbf{E}$

$$\begin{aligned}\mathbf{H}_r(r,\varphi) =& \frac{1}{\omega\mu_0 k_z r}\left[\cos\varphi(\frac{\partial^2 E_x}{\partial r\partial\varphi} + \frac{1}{r}\frac{\partial^2 E_y}{\partial\varphi^2} + \frac{\partial E_y}{\partial r} - \frac{1}{r}\frac{\partial E_x}{\partial\varphi} - k_z^2 r E_y)\right.\\ &\left. + \sin\varphi(\frac{\partial^2 E_y}{\partial r\partial\varphi} - \frac{1}{r}\frac{\partial^2 E_x}{\partial\varphi^2} - \frac{\partial E_x}{\partial r} - \frac{1}{r}\frac{\partial E_y}{\partial\varphi} + k_z^2 r E_x)\right]\exp(jk_z z - j\omega t),\end{aligned} \tag{S4}$$

$$\mathbf{H}_z(r,\varphi) = -\frac{j}{\omega\mu_0}\left[\cos\varphi(\frac{\partial E_y}{\partial r} - \frac{1}{r}\frac{\partial E_x}{\partial\varphi}) + \sin\varphi(-\frac{\partial E_x}{\partial r} - \frac{1}{r}\frac{\partial E_y}{\partial\varphi})\right]\exp(jk_z z - j\omega t). \tag{S5}$$

The time-averaged linear momentum flux carried by the optical field is given by Poynting's theorem as $\mathbf{P} = \langle\mathbf{E}\times\mathbf{H}\rangle/2c^2$. In the cylindrical coordinate system, the azimuthal component of the linear momentum flux, P_φ, is

$$P_\varphi \propto \Re[\mathbf{E}_z\times\mathbf{H}_r^* - \mathbf{E}_r\times\mathbf{H}_z^*], \tag{S6}$$

where $*$ denotes the complex conjugation and $\Re[\cdot]$ indicates the real part. In the cylindrical coordinate system, E_x and E_y can be written as

$$\begin{aligned}E_x(r,\varphi) =& u(r,\varphi)\exp[j\psi(r,\varphi)]\alpha(r,\varphi),\\ E_y(r,\varphi) =& u(r,\varphi)\exp[j\psi(r,\varphi)]\beta(r,\varphi).\end{aligned} \tag{S7}$$

Here $u(r,\varphi)$ and $\psi(r,\varphi)$ represent the spatial distributions of the amplitude and phase, respectively. $\alpha(r,\varphi)$ and $\beta(r,\varphi)$ determine the spatial distributions of the polarization state with $\alpha\alpha^* + \beta\beta^* = 1$. The azimuthal component of the linear momentum P_φ can be decomposed into four categories under the paraxial approximations as

$$\begin{aligned}P_\varphi^{(1)} &\propto 2\frac{1}{r}|u|^2\frac{\partial\psi}{\partial\varphi},\\ P_\varphi^{(2)} &\propto j\frac{\partial|u|^2}{\partial r}(\alpha^*\beta - \alpha\beta^*),\\ P_\varphi^{(3)} &\propto j\frac{1}{r}|u|^2\left(\alpha\frac{\partial\alpha^*}{\partial\varphi} + \beta\frac{\partial\beta}{\partial\varphi}^* - c.c.\right),\\ P_\varphi^{(4)} &\propto j|u|^2\frac{\partial(\alpha^*\beta - \alpha\beta^*)}{\partial r}.\end{aligned} \tag{S8}$$

According to the definition of angular momentum (AM) $\mathbf{j} = \mathbf{r} \times \mathbf{P}$, we can obtain the optical AM in the propagation direction as $\mathbf{j}_z = \mathbf{r} \times \mathbf{P}_\phi$, and j_z can also be decomposed into four categories as

$$\begin{aligned} j_z^{(1)} &\propto 2|u|^2 \frac{\partial \psi}{\partial \varphi}, \\ j_z^{(2)} &\propto jr \frac{\partial |u|^2}{\partial r} (\alpha^* \beta - \alpha \beta^*), \\ j_z^{(3)} &\propto j|u|^2 \left(\alpha \frac{\partial \alpha^*}{\partial \varphi} + \beta \frac{\partial \beta}{\partial \varphi}^* - c.c. \right), \\ j_z^{(4)} &\propto jr|u|^2 \frac{\partial (\alpha^* \beta - \alpha \beta^*)}{\partial r}. \end{aligned} \tag{S9}$$

Here $j_z^{(1)}$ is the well-known intrinsic OAM caused by the vortex phase. Our group had realized OAM $j_z^{(3)}$ associated with the azimuthally varying polarization state of the vector field and OAM $j_z^{(4)}$ arising from the curl of polarization of the vector field. In this work, we focus on $j_z^{(2)}$ and control the local AM density based on the linearly-varying radial phase.

2. CALCULATION OF THE LOCAL AM BASED ON RICHARDS-WOLF INTEGRAL

We can calculate the distribution of focal field by the Richards-Wolf integral, with Eqs. (S4)-(S6)

$$\mathbf{E}_f = \frac{-jkf}{2\pi} \int_0^\alpha d\theta \int_0^{2\pi} \sqrt{\cos\theta} \mathbf{M}_e K(r,\theta) \sin\theta d\phi, \tag{S10}$$

with

$$\mathbf{M}_e = \begin{bmatrix} \left(E_\rho \cos\theta \cos\phi - E_\phi \sin\phi\right) \hat{\mathbf{e}}_x \\ \left(E_\rho \cos\theta \sin\phi + E_\phi \cos\phi\right) \hat{\mathbf{e}}_y \\ E_\rho \sin\theta \hat{\mathbf{e}}_z \end{bmatrix},$$

where $K(r,\theta) = \exp\{jk[z\cos\theta + r\sin\theta\cos(\varphi - \phi)]\}$, f is the focal length of the lens with $NA = n\sin\alpha$ in a medium of refractive index n and α is the convergence angle. ρ and ϕ is the radial and azimuthal coordinates, respectively. $\mathbf{M}_e$ is the polarization vector of the electric field. According to the Maxwell's equations, the electric and magnetic vectors are orthogonal in an isotropic dielectric medium, and the magnetic component can be calculated as

$$\mathbf{H}_f = \frac{-jkf}{2\pi} \int_0^\alpha d\theta \int_0^{2\pi} \sqrt{\cos\theta} \left(\hat{\mathbf{k}} \times \mathbf{M}_e\right) K(r,\theta) \sin\theta d\phi, \tag{S11}$$

where $\hat{\mathbf{k}} = (-\sin\theta\cos\phi, -\sin\theta\sin\phi, \cos\theta)$ is the unit vector of the wave vector. The AM density of the focused field can be calculated by $j_z = \Re[\mathbf{r} \times (\mathbf{E}_f \times \mathbf{H}_f^*)]$. The local integral AM J_z^L experienced by a probe particle can be written as

$$J_z^L \propto \int_{R_P - a}^{R_P + a} j_z dr, \tag{S12}$$

where R_P is the radius of the strongest ring and $a = 1.6\ \mu$m is the radius of the probe particle.

We can simulate the transverse distribution of focal fields using the Richards-Wolf integral. Figure S1 shows the simulated transverse intensity pattern in the x-z plane near the geometric focal plane of the objective with $NA = 0.75$ for the optical field with the linearly-varying radial phase ($q = \pm 7$). As shown in Fig. S2, the transverse intensity patterns of focal fields are the same for $\sigma = \pm 1$ with $q = +6$. However, the local AM densities carried by the optical fields are opposite for orthogonal polarization states.

For a certain spin (for instance, $\sigma = +1$), the radial index q obviously controls the intensity and local AM density. At the same position, the radius of the annular intensity of the focal field increases with the increase of the radial index q, which means that the value of the radial index can control the velocity of the orbital motion, as shown in Figs. S3(a) and S3(e). For $|q| = 6$, the sign of the radian index control not only the transverse intensity pattern, but also determines the sign of the local AM density, i.e. the direction of the orbital motion, as shown in Figs. S3(b) and S3(d). It verifies the radial phase is the effective and flexible method to control the local AM.

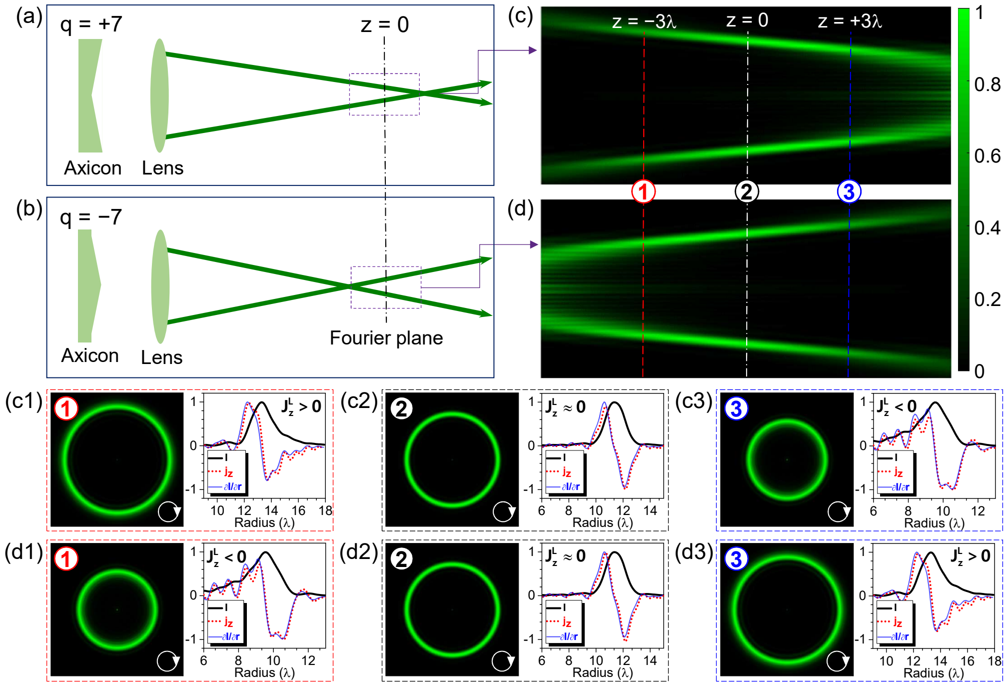

Fig. S1. Simulated transverse intensity patterns, radial-varying intensities, RIGs and local AM densities of focused fields with the linearly-varying radial phase for the right-hand circular polarization $\sigma = +1$. (a) or (b), Schematic diagram of focusing process of optical field with the radial index of $q > 0$ or $q < 0$. $z = 0$ represents the geometric focal plane (Fourier plane) of the objective. (c) or (d), Simulated x-z plane intensity distribution of focused optical field with the radial index $q = +7$ or $q = -7$ in the vicinity of the geometric focal plane of the objective with NA = 0.75 within the range of $z \in [-6\lambda, +6\lambda]$. (c1)-(c3) or (d1)-(d3), Simulated transverse intensity patterns, radial-varying intensities, RIGs and local AM densities at three different planes shown in (c) or (d): ① $z = -3\lambda$, ② $z = 0$, ③ $z = +3\lambda$, in which all the pictures have the same size of $37 \times 37\lambda^2$.

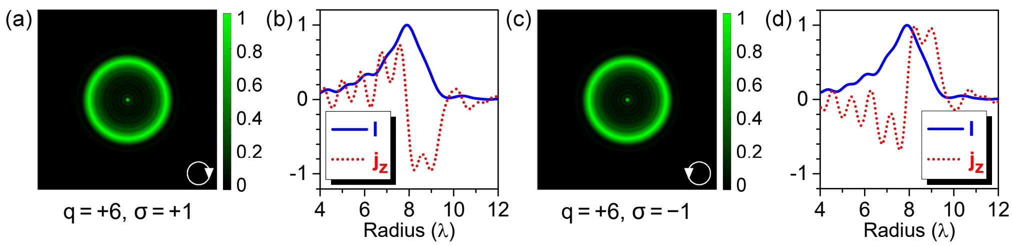

Fig. S2. Simulated transverse intensity patterns, radial-varying intensities, and local AM densities of focused fields for the right- and left-handed circularly polarized fields with the linearly-varying radial phase behind the focal plane of the objective with NA = 0.75. (a) or (c), transverse intensity patterns of focused fields with radial index $q = +6$ for $\sigma = +1$ or $\sigma = -1$ behind the geometric focal plane ($z = +3\lambda$), respectively, any picture has the same size of $37 \times 37\lambda^2$. (b) or (d), radial-varying intensity (blue solid curves) and local AM density (red dotted curves).

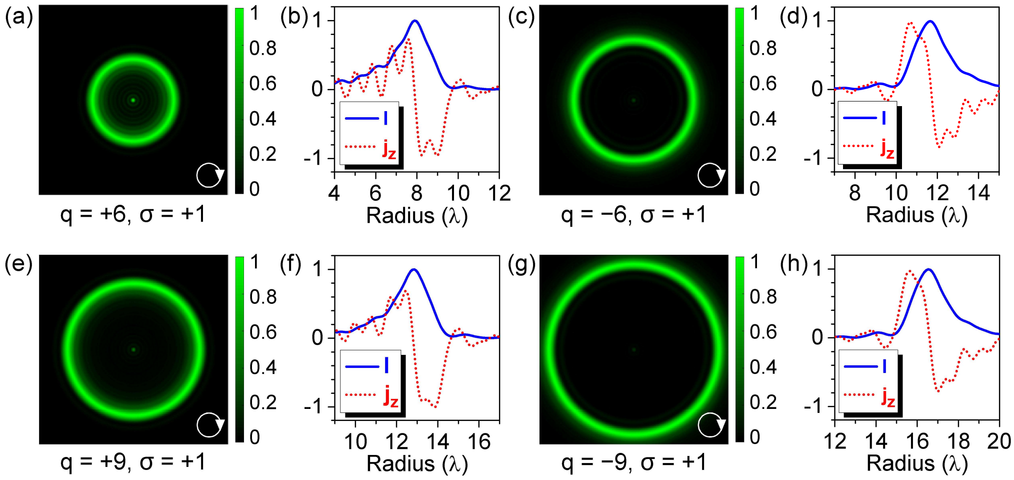

Fig. S3. Simulated transverse intensity patterns, radial-varying intensities, and local AM densities of focused fields for different radial index q behind the geometric focal plane ($z = +3\lambda$). The objective has a NA of 0.75, any picture size has the same size of $37 \times 37\lambda^2$. (a) or (c), transverse intensity pattern of focal field with opposite radial index $q = +6$ or $q = -6$ in the same polarization state ($\sigma = +1$). (b) or (d), radial-varying intensity (blue solid curves) and local AM density (red dotted curves) with opposite radial index $q = +6$ or $q = -6$. (e)-(h) are similar results for $q = +9$ or $q = -9$.

The important feature of the local AM density is position-dependent. We simulate the variation of the transverse intensity pattern, radial-varying intensity and local AM density along the propagation direction for $\sigma = +1$, as shown in Fig. S4. The local integral AM is opposite before and behind the focal plane of the lens ($z = \pm 3\lambda$) which means the sense of the orbital motion of particles become opposite. This is completely different from the Laguerre-Gaussian field, which always exhibits a near symmetric intensity distribution with respect to the strongest ring in any plane along the propagation direction, as shown in Figs. S5. So, this local AM density provides a new controlling method for optical trapping through changing the position of the objective or sample.

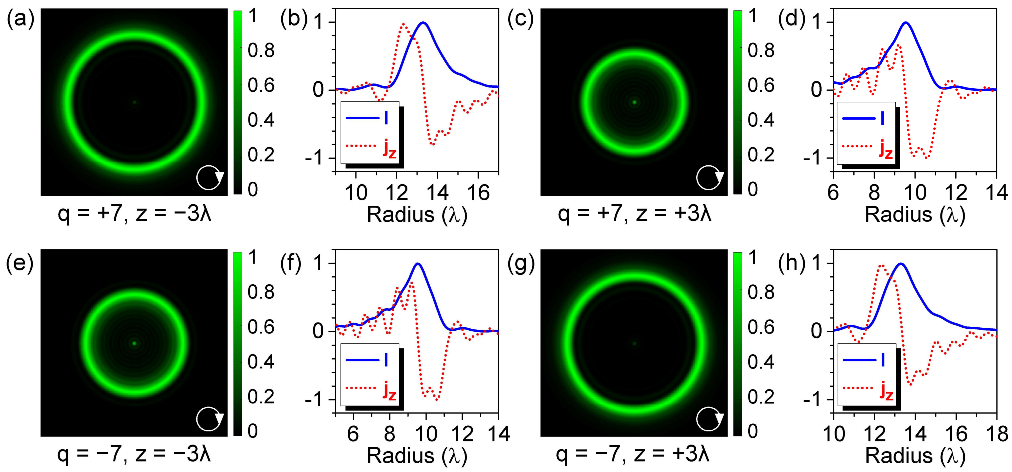

Fig. S4. Simulated transverse intensity patterns, radial-varying intensities, and local AM densities of focused fields for different positions. The objective has a NA of 0.75, any picture size has the same size of $37 \times 37\lambda^2$. (a) or (c), transverse intensity pattern of focal field with radial index $q = +7$ in the same polarization state ($\sigma = +1$) for $z = +3\lambda$ or $z = -3\lambda$. (b) or (d), radial-varying intensity (blue solid curves) and local AM density (red dot curves) for $z = +3\lambda$ or $z = -3\lambda$. (e)-(h) are similar results for $q = -7$.

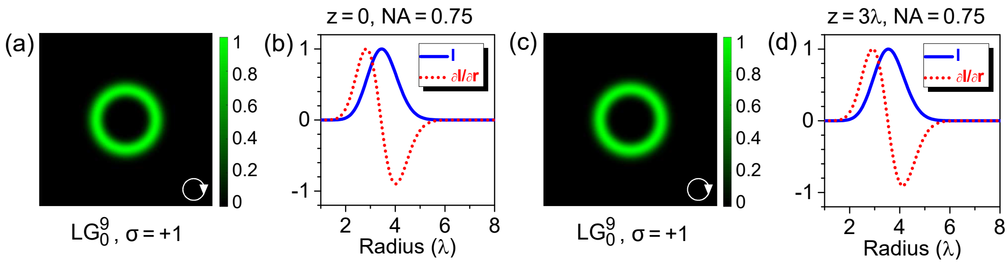

Fig. S5. Simulated transverse intensity patterns, radial-varying intensities, and RIGs of focused fields for the right-handed circular polarized LG mode LG_0^9 ($p = 0$ and $l = 9$) under the strongly focusing condition of the objective with NA = 0.75. (a) and (c), transverse intensity patterns of focused field with the topological charge $l = +9$ for $\sigma = +1$ in the geometric focal plane ($z = 0$) and behind the geometric focal plane ($z = 3\lambda$), respectively, any picture has the same size of $20 \times 20\lambda^2$. (b) and (d), radial-varying intensity (blue solid curves) and RIG (red dot curves), corresponding to (a) and (c), respectively.

In addition, we interest in what is the relationship between the intrinsic OAM and the local AM density, i.e. the relationship between the azimuthal phase and the radial phase of light. We calculate the transverse intensity pattern, radial-varying intensity and local AM density of focused fields with the radial index $q = +6$ and the topological charge $m = +1$ for different polarization $\sigma = \pm 1$, as shown in Fig. S6. We can control the sign of the local AM density by changing the polarization. When $\sigma = +1$, the sum of the AM from the azimuthal phase and the radial phase is close to zero, which means trapped particles do not have the orbital motion and almost stop (see Fig. 6 in the main text). The forces from the helical wavefront and the intensity gradient are canceled. Obviously when $\sigma = -1$, trapped particles will rotate faster because both AM have same sign.

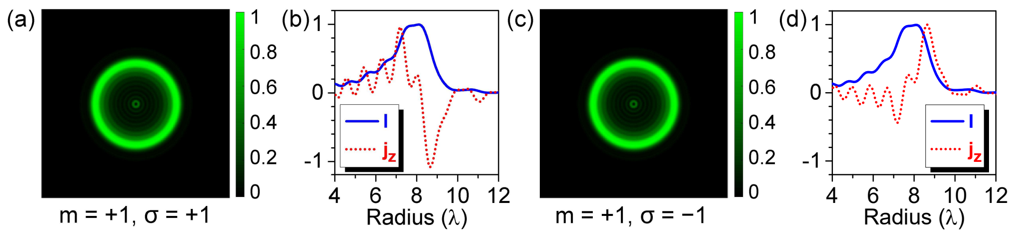

Fig. S6. The relationship between the intrinsic OAM (azimuthal phase) and local AM density (radial phase) behind the focal plane $z = +3\lambda$. The objective has a NA of 0.75, any picture size has the same size of $37 \times 37\lambda^2$. The radial index $q = +6$ and the topological charge $m = +1$. (a) or (c), transverse intensity pattern of focused field for $\sigma = +1$ or $\sigma = -1$. (b) or (d), radial-varying intensity (blue solid curves) and local AM density (red dot curves) for $\sigma = +1$ or $\sigma = -1$.

We also explore the dependence of the orbital motion of particles on spin (Fig. S7). In our work, the spin-orbit interaction also exists, but the intensity of the longitudinal field is very small comparing with transverse field components (Fig. S8), therefore the orbital motion of the microparticle from spin-orbit interaction can be ignored and the RIG plays an important role in the spin-to-orbital conversion in the case of high numerical aperture (Fig. S9).

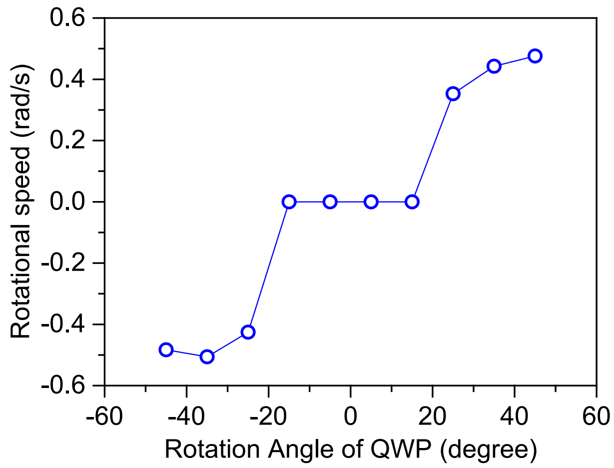

Fig. S7. Dependence of the rotation velocity of trapped microparticles on the orientation angle of QWP. The positive and negative values represent the opposite directions of rotation.

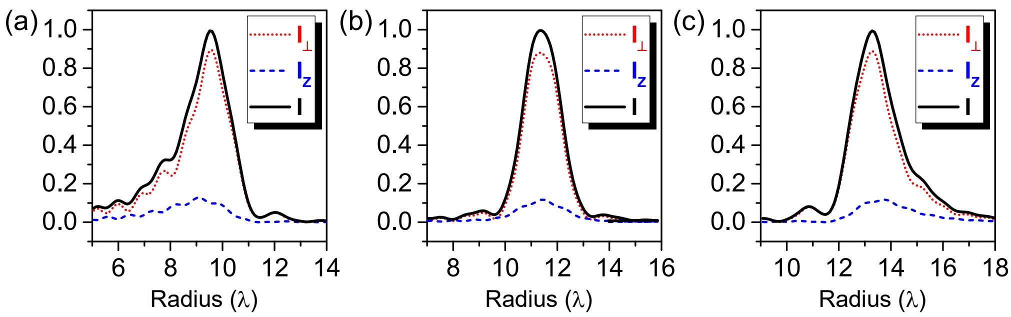

Fig. S8. Radial-varying intensity distributions of the transverse ($I_\perp$, as shown by red curves) and longitudinal (I_z, as shown by blue curves) components as well as the total field (I, as shown by black curves) for focused fields in different planes. The objective has a NA of 0.75, the radial index $q = +7$ and $\sigma = +1$. (a) $z = -3\lambda$, (b) $z = 0$ and (c) $z = +3\lambda$.

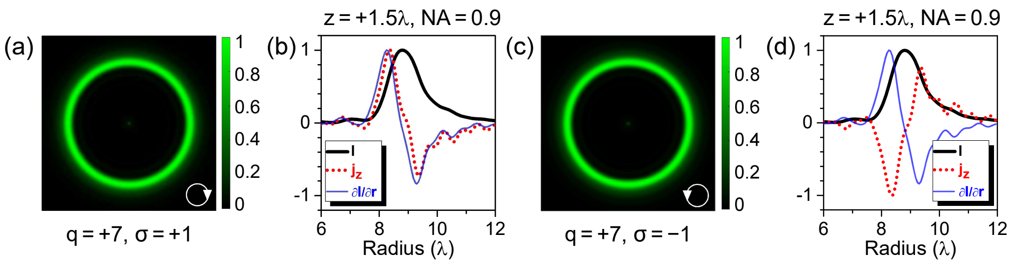

Fig. S9. Simulated transverse intensity patterns, radial-varying intensities, RIGs and local AM densities of focused fields for the right and left-handed circularly polarized fields with the linearly-varying radial phase behind the focal plane of the objective with NA = 0.9. (a) or (c), transverse intensity patterns of focused fields with radial index $q = +7$ for $\sigma = +1$ or $\sigma = -1$ behind the focal plane ($z = +1.5\lambda$), respectively, any picture has the same size of $25 \times 25\lambda^2$. (b) or (d), radial-varying intensity (black solid curves), RIG (blue solid curves) and local AM density (red dot curves).

3. MORE EXPERIMENTAL DETAILS

A. Generation of the optical fields with linearly-varying radial phase

In our experiment, we create the optical fields with linearly-varying radial phase by using a phase-only spatial light modulator (SLM, a reflective phase modulator array of 1920 × 1080 pixels). The transmission function of the blazed grating on SLM is $t(x, y) = \gamma \mod (2\pi f_0 x + \delta, 2\pi)$, where δ is the additional phase distribution, f_0 and γ are the spatial frequency and modulation depth of SLM, as shown in Figs. S10(a) and (b), respectively. For the linearly polarized light, its first-order diffracted light has the phase $\exp(+j\delta)$ with a diffraction efficiency of ∼70%. We set $\delta = \alpha_0 + 2\pi q r/r_0$ for the radial phase, where r represents the radial coordinate and r_0 is the radius of the optical field incident on SLM. α_0 and q are the initial phase and the radial index, respectively. Interfering with the Gaussian beam, the concentric-ring intensity patterns experimentally verify this property, as shown in Fig. S10(c) and (d).

B. Optical tweezers setup

Optical tweezers are capable of manipulating micrometer-sized dielectric particles. Our optical tweezers setup is based on a Zeiss inverted microscope as shown in Fig. S10. A linearly polarized continuous-wave laser (Verdi-5, Coherent Inc.) with a power of 5 W and a wavelength of 532 nm is expanded and collimated by a telescope and is then reflected onto the phase-only SLM (Pluto II, HOLOEYE Photonics AG, Germany). The required optical field is created by the computer generated hologram loaded on SLM, and then passes through a 4f system consisting of two lenses (L1 and L2 with the same focal length of $f = 250$ mm). The input plane of the objective O1 and the SLM plane are the conjugate image planes with each other, by using the 4f system and the telescope system (T). A filter at the Fourier plane of the 4f system blocks all diffraction orders except for the first order. A quarter-wave plate (QWP) is inserted between T and O1 to convert the linearly polarized light into the circularly polarized one. Optical trapping is performed using the inverted microscope (Zeiss observer Z5) with the objective O1 (60× and NA = 0.75). The particles used for optical trapping in experiment are neutral isotropic colloidal beads of 1.6 μm in radius and were dispersed in sodium dodecyl sulfate solution in the cell with glass coverslip. The image of the trapped particles are observed another objective O2 (100× and NA = 0.95). Two charge coupled device cameras CCD1 and CCD2 with resolution of 1280 × 1024 pixels and maximum frame rate of 60 fps are used to record the manipulation process of the trapped particles.

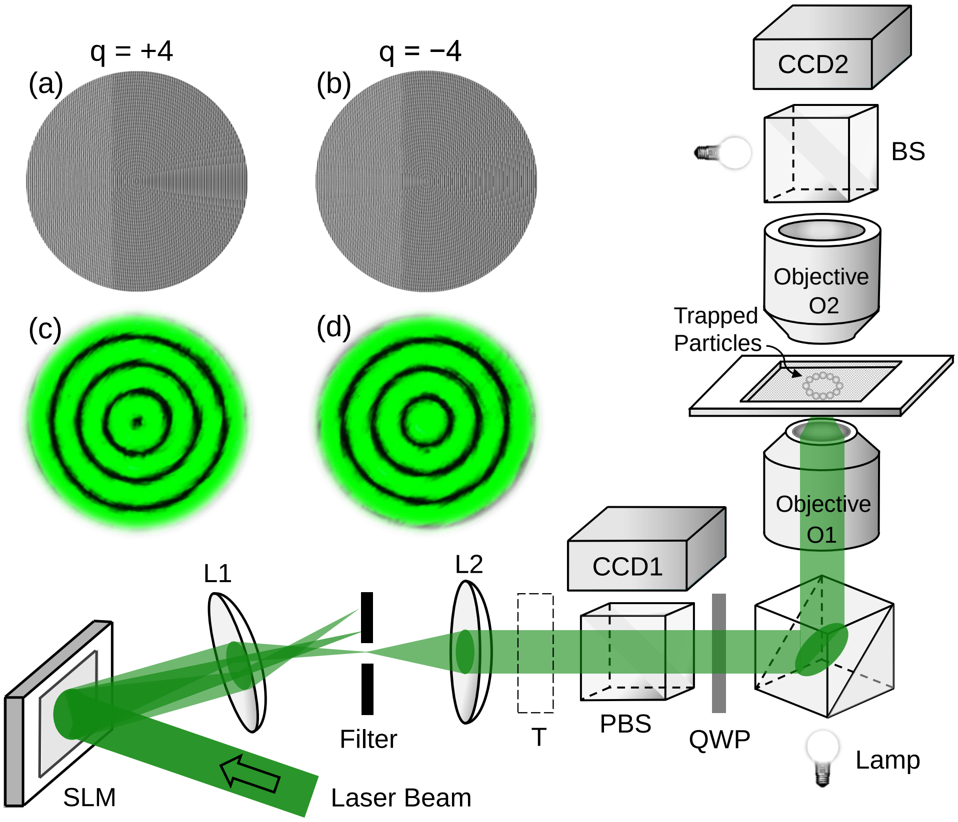

Fig. S10. Experimental setup of optical tweezers for validating the local AM based on linearly-varying radial phase. SLM is a phase-only spatial light modulator loading blazed gratings, T is the telescope system, PBS is polarization beam splitter and QWP is a quarter-wave plate to change the spin. Inset shows the blazed gratings (a) and (b) loaded on SLM with different linearly-varying radial phase (radial index $q = \pm 4$) and the intensity patterns of interference (c) and (d) between the optical fields with radial index ($q = \pm 4$) and the fundamental Gaussian mode.